Mechanical characterisation and crashworthiness performance of additively manufactured polymer-based honeycomb structures under in-plane quasi-static loading

Isaac, C. W., Sokołowski, A., Duddeck, F., Adamiak, M., Pakieła, W. & Aremu, D

Mechanical characterisation and crashworthiness performance of additively manufactured polymer-based honeycomb structures under in-plane quasi-static loading

Chukwuemeke William Isaac [a], Andrzej Sokołowski[a], Fabian Duddeck[b], Marcin Adamiak[c], Wojciech Pakieła[d] and Adedeji Aremu[e]

[a]Faculty of Mechanical Engineering, Department of Machine Technology, Silesian University of Technology, Gliwice, Poland; [b]TUM School of Engineering and Design, Technical University of Munich, Munich, Germany; [c]Faculty of Mechanical Engineering, Materials Research Laboratory, Silesian University of Technology, Gliwice, Poland; [d]Department of Engineering Materials and Biomaterials, Faculty of Mechanical Engineering, Silesian, University of Technology, Gliwice, Poland; [e]School of Mechanical Engineering, Faculty of Engineering, Coventry University, Coventry, UK

ABSTRACT

Additive manufacturing technology is suitable for producing energy-absorbing devices with tunable mechanical properties and improved crashworthiness performance. In this study, the mechanical properties and macrostructural crushing behaviour of five additively manufactured polymer-based honeycomb structures (HS) are investigated. Subjected to in-plane loading, the experimental results of the HS are compared with numerical findings and theoretical predictions. Results indicate that deformation modes and overall crushing performance are influenced by utilising different parent materials. The polymer HS made from polyethylene terephthalate glycol gives the best overall crushing performance over the other polymers and polymer-fibre reinforcement HS. However, the crush force efficiency of HS made from polylactic acid is the least promising. The polymer-fibre reinforced HS outperforms some of the pure polymer-based ones in terms of specific energy absorption and shows a characteristic lightweight advantage. Hence, spotting it as a promising energy absorber utilised for crashworthiness application especially where ultra-lightweight property is highly desired.

1. Introduction

Energy absorbing structures are used as protective device incorporated into vehicular structures to protect carriers, passengers carried and/or cargoes transferred, from mild and catastrophic damages or injuries during impact or crash scenarios. To this end, various studies have looked at ways of designing more efficient energy absorbing structures using different structural designs [1–6]. For example, a structural design mimicked from nature is the honeycomb structure. This nature-inspired structure, has lightweight advantage, high specific strength and stiffness making it an excellent energy absorbing device currently applied in the aerospace, marine, automotive and building industrial sectors. However, certain factors including the fabrication techniques for realising the structure, the kind of structural designs and the type of materials used, can either increase or decrease the efficiency of the honeycomb structural absorber, significantly. First, several manufacturing techniques including the subtractive manufacturing technique, have been used to fabricate the honeycomb energy absorbing structures [7–9]. However, these techniques have suffered some challenges in designing lightweight and more complex structures. The introduction of additive manufacturing has not only overcome these challenges but also provide novel possibilities of fabricating complex structures with special functionalities [10–12]. Second, different geometrical and topological honeycomb structural designs have emerged in recent times through the modification of their vertices and cell walls [13,14] to produce honeycomb structures with negative, zero and positive Poisson ratios [15–20]. Third, materials utilised for producing the honeycomb structures are typically obtained from polymers, composites, ceramics, metals and alloys. The mechanical property of these materials is one of the major factors to be considered when designing and fabrication an effective honeycomb structure. In this study, the

mechanical properties of a composite-based and some polymer-based materials are characterised.

In many cases, the mechanical properties of the feedstocks for additive manufacturing are indicated by the suppliers. However, the conditions under which these material feedstocks were initially tested are seldom provided. Research findings showed that there could be significant variation in the values given by the supplier and those determined by the executors. For example, it was shown by [21] that the material properties of ABS-plus provided by the supplier were different from those obtained by the authors. In the authors' findings, values of the ultimate tensile strength, Young's modulus, yield strength and fracture strain were 7.1%, 5.2%, 3.2% and 3.3% different from those given by the supplier of the ABS-plus feedstock. Moreover, these properties can further be influenced by the process parameters of the 3D printing techniques. Therefore, it is of utmost importance to test the actual mechanical property of the base materials according to prescribed standards. The data obtained via the material testing not only help investigators to know the actual mechanical properties of the 3D printed parts but can also be incorporated into numerical simulations of structural parts. The results of the numerical approximations can be utilised to virtually validate the 3D printed parts.

The emergence of additive manufacturing, also referred as 3D printing, has made possible the fabrication of both simple and complex structural parts. These parts are obtained by adding materials in successive layers until the build parts are completely formed. A good number of 3D printing techniques [22–27] including material extrusion, for example, fused deposition modelling (FDM) or fused filament fabrication (FFF), have been utilised to realise cellular structures for energy absorption [28–31]. In the present study, the FFF 3D printing technology is used to fabricate all the cellular honeycomb structural parts investigated. The FFF technique uses the principle of material extrusion [32]. That is, the feed materials are first heated and then extruded by the nozzle before depositing them layer-by-layer on the build platform. In recent times, quite a good number of researchers have used the FFF technique to fabricate honeycomb structures for energy absorption [33–37]. To mention a few, Habib et al. [38] used the FFF technology to fabricate honeycomb structure made from nylon material. The structures were subjected to both in-plane and out-of-plane compression and their energy absorption capacities were investigated. Using similar material specimen (i.e. nylon), Alomarah et al. [39] utilised the FFF technique to fabricate hexagonal and re-entrant honeycomb structures and compared them with re-entrant chiral auxetic

structure. The fabricated structures were compressed in the in-plane and out-of-plane loading directions and their crushing performance were compared and evaluated with respect to their loading conditions. In a more recent investigation, Li, Sun et al. [40] studied the compression behaviour and energy absorption of FFF fabricated honeycomb structures made from PLA material and having varying cross-sections. Their investigation showed that under in-plane quasi-static compression, variable cross-sections such as change in cell topologies, flip angles and symmetry modes of the honeycomb structures influenced their crushing performance.

The parts produced via FFF technology can be influenced by various printing parameters including build platform, raster lay-up, printing orientation, layer height, nozzle speed, nozzle diameter, infill density, etc. For example, Domínguez-Rodríguez et al. [41] investigated the effect of infill densities and printing orientation on the mechanical performance of ABS honeycomb structures fabricated by the FFF techniques. Ma et al. [42] studied the influence of infill pattern, infill density and material types on the crushing performance of PLA and PLA/carbon fibre based FFF 3D printed cubes. Lubombo and Huneault [43] studied the effects of five infill patterns using three infill densities, on the mechanical response of cellular PLA parts manufactured via the FFF technology. Khosravani et al. [44] analysed the effects of raster orientation and printing speeds on the mechanical properties of 3D printed PLA parts fabricated via the FFF technology. From the investigations carried out by these researchers, it can be seen that the printing parameters significantly influenced the mechanical properties and crushing performance of the 3D printed parts. In the present study, various material specimens are investigated and the effects of infill densities on the 3D printed parts are analysed. This is motivated by the following aspect.

Therefore, it is seen that most researchers only investigated the material properties and crushing performance of additively manufactured parts or honeycomb structures made from either single or dual materials. Very few research works have been carried out to characterise different materials, reveal their material microstructures and compare their macrostructural in-plane crashworthiness performance at the same time which is to the opinion of the authors essential. In this study, four polymer-based materials which include polylactic acid (PLA), polyethylene terephthalate glycol (PETG), acrylonitrile butadiene styrene (ABS) and acrylonitrile styrene acrylate (ASA) and one polymer-fiber reinforcement material made from Polyamide 12 with nano-carbon fiber (NCC) are utilised to fabricate dog-

bones and regular hexagonal honeycomb structures via the FFF technology. The study gives some description of the geometry, material, and fabrication procedures. It further relates the microstructures of the parent materials to their mechanical and crushing performance. Also, it compares and shows both the experimental and numerical results of force-displacement characteristics, deformation modes and crushing performances of the honeycomb structures made from five selected materials. Lastly, numerical approximations and experimental measurements are used to compare the theoretical predictions of the crushed honeycomb structures.

2. Methodology

2.1. Specimen geometric description

In this study, a regular honeycomb structure whose 3D CAD design dimensions as illustrated in Figure 1 is adopted. Various materials are tested with the same geometric and parametric conditions. The honeycomb structure is chosen for the study because of its bio-inspired nature and wider application as cellular energy absorbers for impact and crushing mitigation. Figure 1(a) shows the unit cell of the honeycomb with thickness t and length of each side l having six equal sides. Its length, width and height are designated as a_x, a_y and a_z, respectively as shown in Figure 1(b). Table 1 gives the geometric parameters of the regular honeycomb structure. Printing of the honeycomb structure was realised on the $xy-$plane and built along the $z-$direction as seen in Figure 1(b). The dimensions of the printed honeycomb structures were slightly different from the CAD model due to the limitation in accuracy of the FFF printer. Loading along the build direction (i.e. $z-$direction) is referred as out-of-plane crushing, designated as v_z in Figure 1(c). However, loading along the xy printing plane, (i.e. either in x-direction or $y-$direction) is referred as in-plane crushing, designated as v_x or v_y, respective as depicted in Figure 1 (c). In this study, we focus only on the in-plane crushing along the $x-$direction, hereafter called in-plane crushing.

As mentioned, all specimens have approximately same dimensions and are made from five different material filaments. The measured relative density is given as
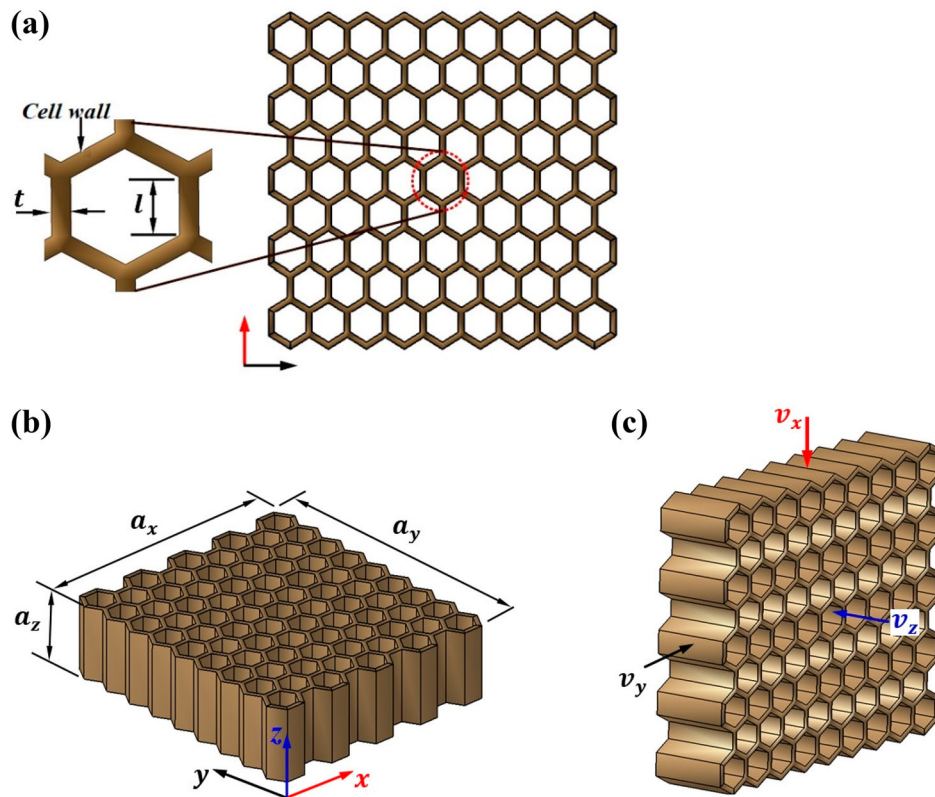
$$\rho_M^* = \frac{\rho_s}{\rho_m} \tag{1}$$

Figure 1. CAD model (a) 2D view of honeycomb structure with the exploded view of its cell wall (b) 3D view of honeycomb structure showing its dimensions, xy printing plane and build direction along the z-axis (c) 3D view of honeycomb structure showing in-plane crushing in x- and y-directions, and out-of-plane crushing in z-direction.

Table 1. CAD model geometric parameters of the regular honeycomb structure used in this study.

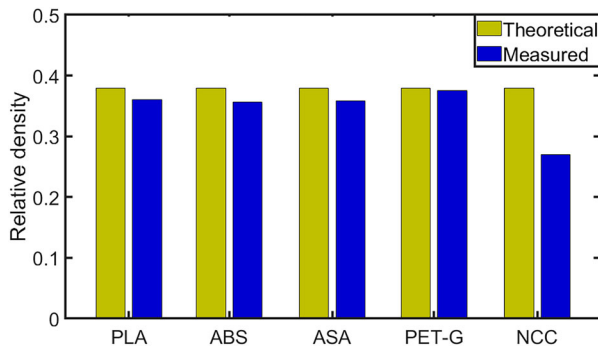| Parameters (mm)	Symbols	Values
Length	a_x	119.0
Width	a_y	107.3
Height	a_z	25.0
Side	l	7.5
Wall thickness	t	2.0

where ρ_s is the ratio of the mass of the honeycomb structure to the volume of the material configuration. The average density of the honeycomb structures made from PLA, ABS, ASA, PETG and NCC are approximately 446.40, 372.75, 385.56, 448.95 and 377.99 kg/m^3, respectively. Also, ρ_m is the density of the base or parent material. The relative error in the relative density for PLA, ABS, ASA, PETG and NCC are 0.19, 0.05, 0.07, 0.19 and 0.29, respectively. From the regular hexagonal unit cell as depicted in Figure 1(a), the theoretical relative density is the ratio of the area of the cell walls to the total area of the hexagonal unit cell evaluated as [45]

$$\rho_T^* = \frac{4t}{9l}\left(2\sqrt{3} - \frac{t}{l}\right) \tag{2}$$

A comparison between the theoretical and measured relative densities of the different material specimens is depicted in Figure 2. It is seen that ρ_T^* approximates ρ_M^* and hence, verifies the relative densities of the measured results for the different material specimens.

2.2. Material and fabrication procedures

To remove moisture and to improve the mechanical response as well as quality of the printed specimens for the different selected parent materials, each feedstock material was initially pre-heated in a 3D printing dryer. The heating temperature for the material feedstocks ranges from 50 °C to 55 °C and takes an average of 3–6 h of drying as prescribed by the manufacturer. All the polymer-based filaments were obtained from Fiberlogy[1] while the composite-based filament was obtained from F3Dfilament in Poland[2]. The normative diameter of all the filaments used for this study is 1.75 mm. It is worth noting that the nano-carbon filament is a composite of polyamide 12 and nano carbon fibre. After the drying procedure, the heated filaments were transferred to the 3D printer.

All specimens used for setting the printing parameters were modelled using the CATIA V5 CAD software. First, the specimens were simulated in the Ultimaker Cura software. The specimens were 3D printed using the FFF 3D printer which is a dual extruded type produced by TENLOG® 3D solution. This printer has two direct extruders each with nozzles of 0.4 mm that enables the deposition of the extruded filament on the platform surface in a layer-by-layer manner as illustrated Figure 3. All the specimens (i.e. dogbones and honeycomb structures) were printed in the xy−plane with the build direction along the z-axis. Depending on the material to be fabricated and their printing temperature, various techniques of bed adhesion were adopted as recommended by the manufacturer. For example, for satisfactory adhesion, the build platform made from glass material could require either a hairspray, a sticky glue, a masking tape or their combination. Moreover, when using ABS printing material, an enclosed chamber was installed for the 3D printer which ensured the adhesion of the printed specimens. The temperature in the enclosed chamber was maintained

Figure 2. Comparison between measured relative density (ρ_M^*) and theoretical relative density (ρ_T^*) for the various materials used in this study.

Figure 3. Layer-by-layer printing of the honeycomb structure.

Table 2. FFF printing parameters for the various parent materials used in this study.

Printing parameters	PLA	ABS	ASA	PETG	NCC
Nozzle temperature (°C)	220	260	260	250	260
Bed temperature (°C)	70	110	110	90	110
Layer height (mm)	0.3	0.3	0.3	0.3	0.3
Nozzle diameter (mm)	0.4	0.4	0.4	0.4	0.4
Printing speed (mm/s)	60	40	70	80	45
Infill-density (%)	20, 40, 60	20, 40, 60	20, 40, 60	20, 40, 60	20, 40, 60

[1]https://fiberlogy.com; [2]https://f3dfilament.com.

at 43°C and the fan speed of the printer was put for 0% to prevent cooling of the adhered surface. However, for all other printing materials, a closed chamber was not required to produce the printed specimens. Table 2 provides the process parameters utilised for printing the different material specimens. These parameters (i.e. nozzle temperature, bed temperature and printing speed) are obtained from the range of values specified for each material feedstock as recommended by the manufacturer of the FFF printer. The layer height of 0.3 mm is the default value fixed for all materials.

2.3. Specimen material characterisation

A Zwick/Roeu universal tensile machine with a load cell of 10 kN was used to carry out the tensile tests of various material dogbone specimens and mounted as shown in Figure 4(a). For the five material specimens, three infill-densities denoted as d_1, d_2 and d_3 (i.e. 20%, 40% and 60%, respectively) were investigated as illustrated in Figure 4(b). However, it is worth nothing that the infill-density does not consider the thickness of the outer layer generated during the 3D printing. Also, for all dogbone specimens, the percentage of infill layer thickness was set to 100% to ensure that the property of the actual material was retained irrespective of the differences in the values of infill-densities. To ensure standards, the original thickness (t_0) of the dogbone corresponds to the thickness (t) of the honeycomb cell wall. A schematic of the dogbone with the designed parameters is depicted in Figure 4(c). Where A_s is the sectional area, $l_g = 20$ mm represent the grip length, $l_0 = 70$ mm is the gauge length, $l_s = 130$ mm is the overall length, $r_f = 20$ mm is the fillet radius, $w_0 = 10$ mm is the original width, and $w_g = 20$ mm is the grip width. Figure 4(d) depicts the dogbone samples of the different materials after tensile tests. The tensile tests of all the polymer-based materials were performed according to test standard ASTM D638-14 for plastics with thickness above 1 mm. For the composite-based material, testing was done according to the standard test ASTM D3039. To ensure repeatability, two of each sample for the three infill-densities were tested for all material specimens and the average nominal stress–strain graphs are plotted. These graphs and the influence of infill-densities on the mechanical properties for the various base material specimens are discussed in the subsequent sections. Moreover, Table 3 gives the material properties of all tested material specimens.
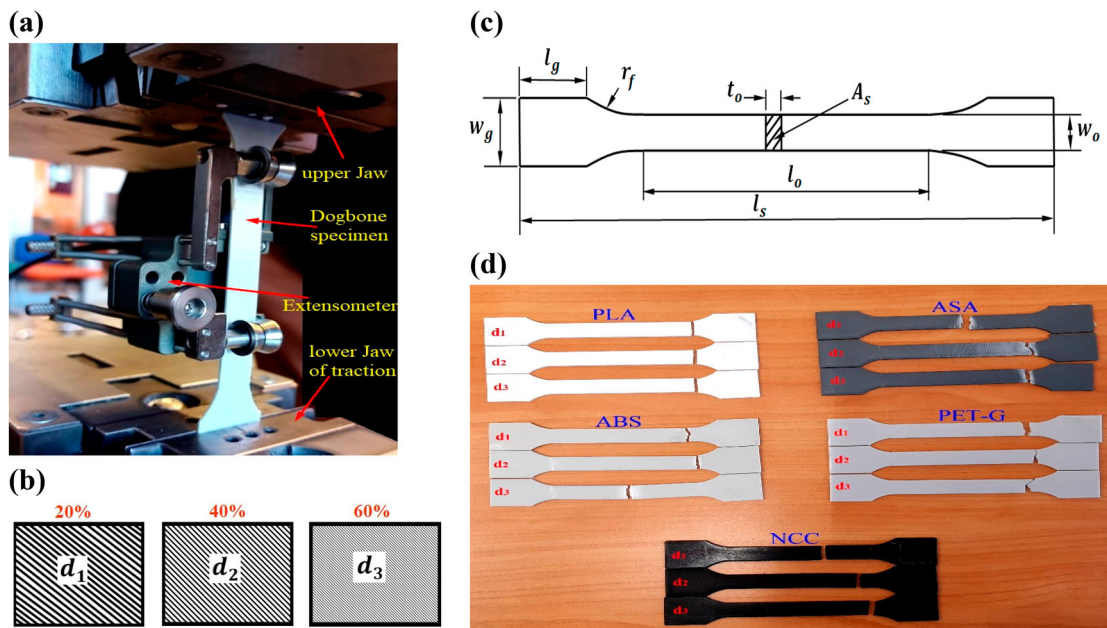

Figure 4. (a) Mounting of universal tensile machine for the tensile tests of dogbones (b) schematic of various infill-densities described in this study (c) schematic and dimensional representation of dogbone (d) various material dogbone specimens after tensile tests.

Table 3. Material properties obtained for the various printing feedstocks utilised in this study.

Material	Density (kg/m2)	Infill-density	Young's modulus (GPa)	Yield stress (MPa)	Ultimate tensile stress (MPa)	Failure strain (%)
PLA	1240	d_1	2.23	45.26	56.50	2.89
		d_2	2.20	44.93	55.74	3.00
		d_3	2.48	49.28	59.21	2.67
ABS	1050	d_1	1.16	24.56	29.00	2.87
		d_2	1.45	30.37	38.26	3.01
		d_3	1.40	29.38	36.58	3.02
ASA	1080	d_1	1.07	22.71	27.69	3.28
		d_2	1.01	21.56	28.40	3.87
		d_3	0.81	17.22	27.22	4.96
PETG	1230	d_1	1.70	34.52	51.77	3.67
		d_2	1.70	34.94	54.02	4.05
		d_3	1.74	35.49	54.66	3.84
NCC	1400	d_1	2.13	43.73	57.02	3.90
		d_2	2.22	44.96	56.60	3.62
		d_3	2.31	46.73	60.06	3.88

2.4. Microstructure features of parent materials

Understanding the microstructure features of the parent materials used in this study can further help in tailoring their mechanical properties toward the design of effective energy-absorbing structures. To this end, the microstructure of various materials utilised in the present work was examined by using an inverted microscope with optical bench at a room temperature of 20°C. The microscope technique involves focus staking the fracture surface of the dogbone specimens after the tensile test have been carried out. Figure 5 shows the micrograph images of the various materials. These
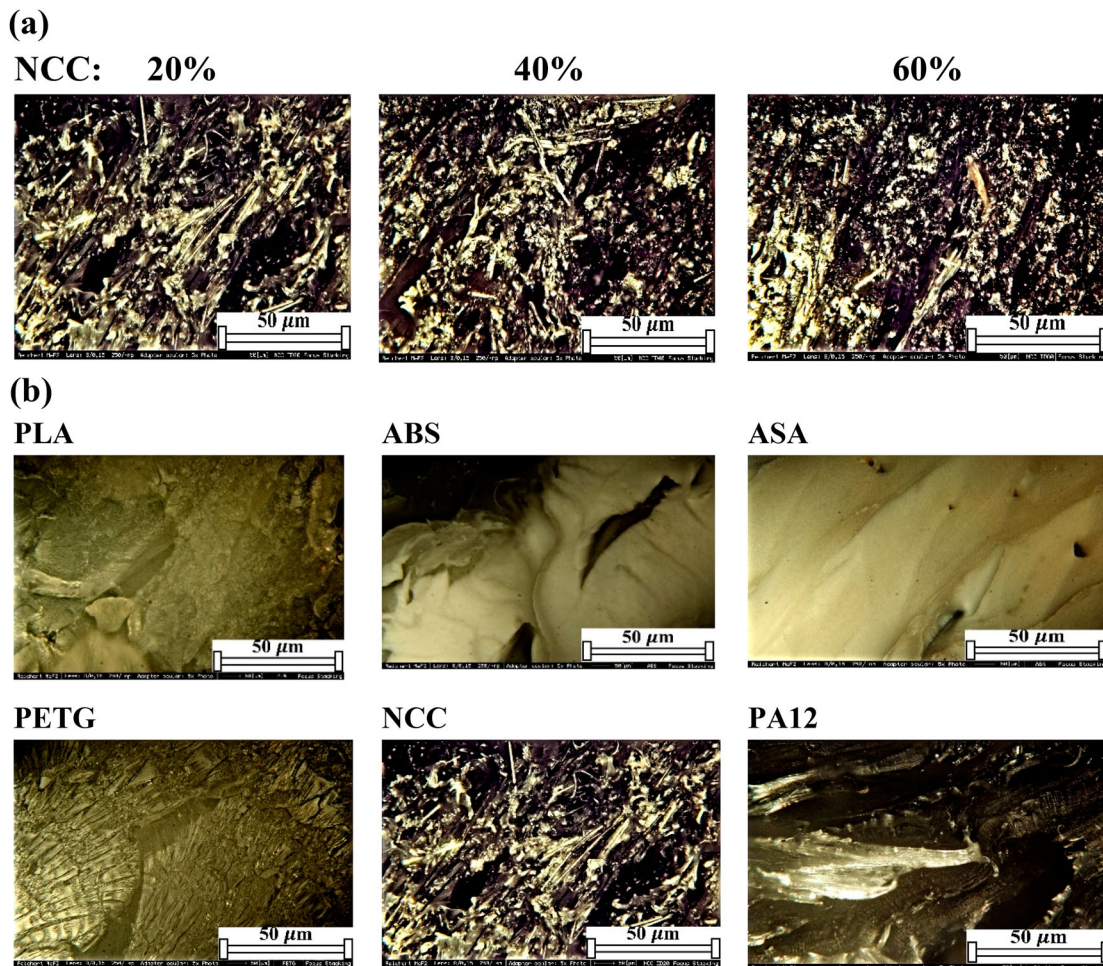
Figure 5. (a) Comparison of the effect of various infill-densities on the microstructure of NCC material (b) Microstructures of parent materials used in this study with a comparison between NCC and PA12 materials.

images are obtained at a direction of 45 degrees perpendicular to the elongation of the dogbone specimens test samples. It was observed that the different infill-densities studied for all material specimens did not play any significant role in their microstructural features. To buttress this point, an illustration is given in Figure 5(a) for NCC material. The three infill-densities show similar microstructures when placed at three different separation areas of the inverted microscope. However, it is evident that various materials have unique microstructural features. To start with, the NCC microstructure, as shown in Figure 5(b), reveals its composite feature i.e. spikes of reinforcement nano-carbon fibres in bright colours and its polyamide 12 (PA12) matrix in dark colours. For the purpose of comparison, the micrograph of a pure PA12 dogbone specimens is also shown alongside with the NCC micrographs in Figure 5(b). In succinct, the PA12 microstructure reveals its highly stretching property. The microstructures of PLA and PETG look similar with PLA more granular-like at the lower left end of the micrograph. Micro-cracks are observed along the polymer boundaries of the PLA material which could explains why PLA materials are highly brittle. On the other hand, the micro-cracks of PETG material are observed to be perpendicularly to the polymer boundaries which could be a reason for their more ductile property. Furthermore, the microstructure of ABS and ASA look very similar in their material flow along polymer boundaries. The presence of micro-cracks along the polymer boundaries for both materials make them more brittle. However, along the polymer boundaries, the ABS material flows less than the ASA material due to some micro-cracks perpendicular to the polymer boundaries. This could be one of the reasons why the ABS material could switch property from being brittle to being ductile. In summary, it can be inferred that the unique microstructural features of the different parent materials have some influences on both the mechanical behaviour and crushing performance of honeycomb structures.

2.5. In-plane compression testing

All the 3D printed honeycomb structures were subjected to quasi-static in-plane loading of 2 mm/min and compressed up to 50% displacement using a Zwick Z100 electronic universal crush test machine as shown in Figure 6(a). This quasi-static speed was selected to easily control and carefully observe the collapse behaviour of the honeycomb structure. The upper platen moves with the quasi-static speed, while the lower platen was fixed. The test machine has a load cell of 100 kN. The honeycomb specimens, as represented in Figure 6(b), were crushed between two circular platens whose diameters are wider than the breadth of the honeycomb structure. This was necessary to capture the true deformation stages of the impacted structure up to $\varepsilon = 0.5$ strain deformation. A 50% plastic deformation was chosen to avoid the onset of densification which is typically associated with rapid increase of force, and consequently, causing the crush test machine to stop abruptly. The crushing distance of the specimens is $D_\delta = \varepsilon a_x$. Deformation stages were captured by a positional high-speed camera and the crushing forces versus displacements were recorded. To confirm repeatability, two samples for each material specimen were tested. Unlike the dogbone specimen with three tested infill-densities for each material specimen, the honeycomb structure, on the other hand, was only tested with 20% and 40% infill-densities. This is because the two infill-densities selected (i.e. 20% and 40%) took lesser time and materials to fabricate compared to the 60% infill-density which required longer period and more material costs to fabricate a sample of the honeycomb structure. As stated previously, the infill-density does not consider the thickness of the outer layer of the 3D printed part. However, for the cellular honeycomb structure, the infill-density takes into consideration the thickness of the inner layer.

2.6. Crushing performance index

The performance of the crushed honeycomb structure is determined by certain crushing indices which can be obtained from the force-displacement curve. Three stages are typically obtained during crushing which are the elastic, plateau and densification stages [14]. However, in this work, only the first two stages are considered. From the force-displacement diagram, the first
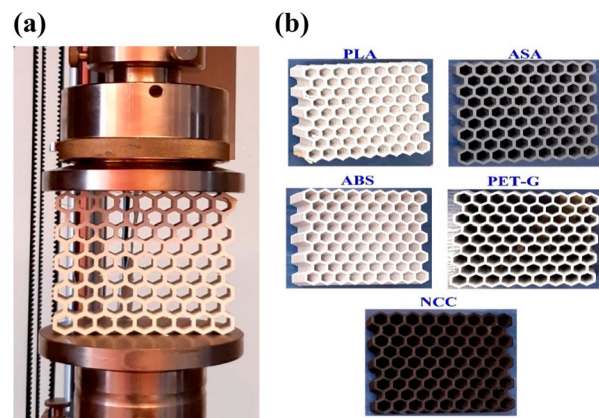

Figure 6. (a) Universal crushing test machine showing the honeycomb structure before in-plane crushing (b) the different material honeycomb specimens investigated in this work.

peak after the elastic stage is referred as initial peak load/force (*IPF*). The lower the *IPF* to the subsequent peaks, the more effective the energy absorber. Moreover, the area under the curve is the energy absorption (*EA*) which is expressed as

$$EA = \int_{0}^{D_\delta} F_L(x)dx \quad ; \qquad (3)$$

where F_L is the crushing force, x is the displacement and D_δ is the crushing distance. The energy absorbed per unit mass is called the specific energy absorption (*SEA*) written as

$$SEA = \frac{EA}{m_c}; \qquad (4)$$

where m_c is the total crushed mass of the structure.

The mean crushing load can be obtained by dividing the energy absorption with the crushed distance of the material specimen. It is calculated as

$$MCL = \frac{EA}{D_\delta}; \qquad (5)$$

Dividing the *MCL* by the peak crushing force/load (*PCF*) gives the crush force efficiency (*CFE*). It is this crushing

index that is used to distinguish the best crushing performance of the different crushed honeycomb structures. The higher the *CFE* the better the crushing performance. Which implies a reduction in force fluctuation during impact loading. This index can be expressed as

$$CFE = \frac{MCL}{PCF} \qquad (6)$$

3. Experimental results and analysis

3.1. Mechanical properties of parent materials

To characterise the different materials by using the dogbone specimens, it was ensured that the differences in infill-densities do not affect the actual materials. Further investigation showed that the fabrication of the dogbone specimen with a 100% infill-density produced similar print with those considered in this study. However, there could be some slight variations in the results during the tensile tests which are discussed in this section. In Figure 7, it is seen that the dogbone specimen made from PLA material with d_3 gives the highest yield stress value and lowest failure strain
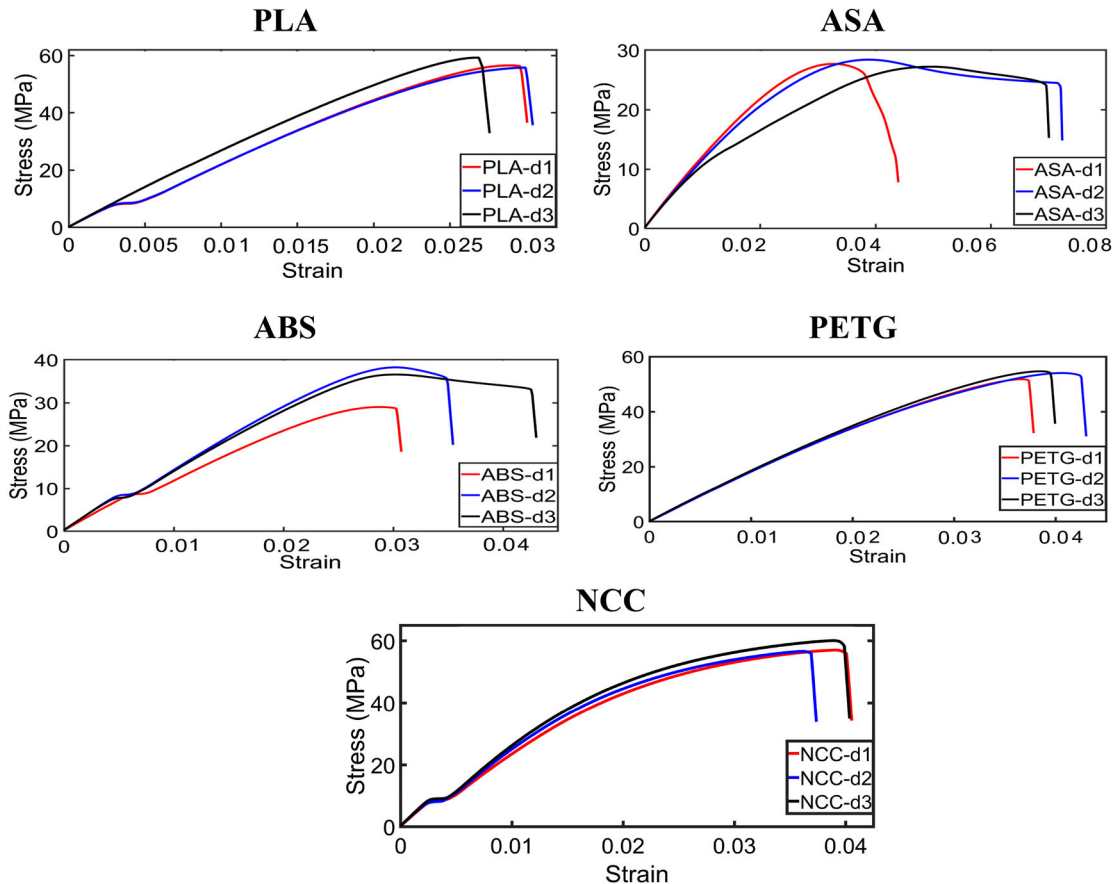
Figure 7. Relationship of stress-strain curves of all the material specimens with the three infill-densities for each material specimen.

value as recorded in Table 3. However, a reduction of infill-density from d_2 to d_1 causes a reduction in the yield stress but significantly elongates yielding of material. For the dogbone specimen made from ABS, the infill-density has some effect in terms of elongation during yielding of the material. The specimen with d_1 shows the least yield stress value. For ASA dogbone specimen, a very low yield stress can be observed with highest failure strain compared to that of PLA and ABS material specimens. For PETG material specimen, it is shown that the infill-densities have very little effect on the dogbone specimen which are observed in their elongation during yielding. For NCC dogbone specimen, the influence of infill-density can be seen both in the yield stress and ultimate tensile stress. A careful selection of infill-densities during 3D printing is, therefore, required especially when there are different materials to choose for specific applications. Moreover, it can be seen that the yield strength of both PLA and NCC materials are relatively higher than those of ABS, PETG and ASA. This indicates that PLA and NCC materials

can withstand higher stresses than their other three material counterparts without them permanently deformed. This attribute makes them promising shape memory polymer feedstocks that could be used for the fabrication of 4D printed energy absorbers with shape changing and recoverability properties [46].

3.2. Force-displacement curve

Figure 8 represents the force displacement curve of all the crushed honeycomb structures. A comparison of the two infill-densities for different materials is also depicted. For the PLA honeycomb structure in Figure 8 (a), the first three peak curves take a regular pattern up to a deformation of 30% compression. Afterwards, the subsequent peak forces behave in irregular way. However, it is seen that the IPF is higher than the subsequent peaks. This force-displacement attribute makes the PLA structure less efficient as crushing absorbers. Additionally, the effect of infill-densities is significant at the initial crushing stages through the peak
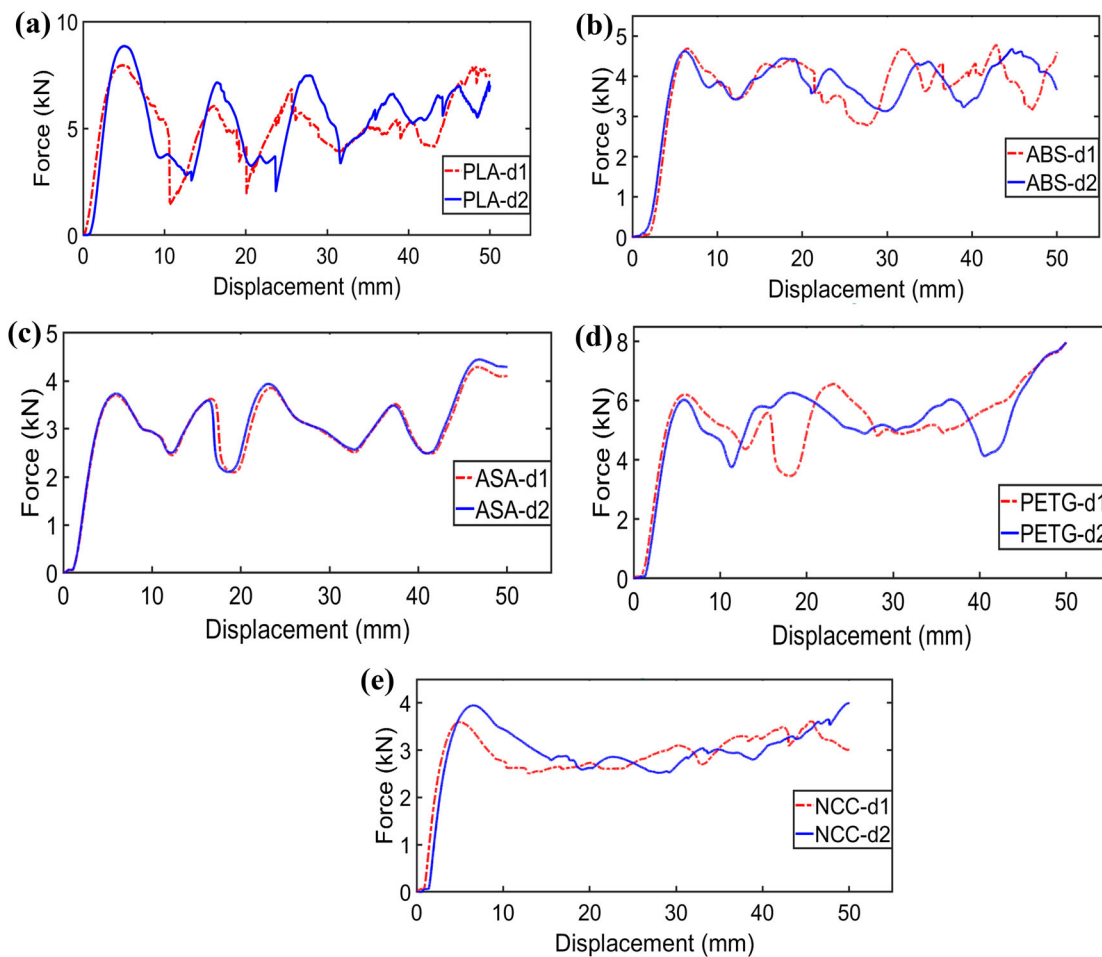
Figure 8. Comparison of force-displacement characteristic curves for the various honeycomb structural specimens with two infill-densities for (a) PLA (b) ABS (c) ASA (d) PETG (e) NCC.

forces and to the final deformation stages. For the ABS honeycomb structure as seen in Figure 8(b), up to 20% deformation, the deformation curves for the two infill-densities behave almost in the same way. After this deformation points, irregular deformation pattern can be observed, and the effect of infill-densities becomes evident on the force-deformation curve. Moreover, the initial peak forces almost correspond to the subsequent peaks which makes the ABS honeycomb structure more promising for crushing absorbers than their PLA counterpart. The force-deformation curve of the two in-fill density in the case of ASA honeycomb structure, show a similar pattern as seen in Figure 8(c). This implies that infill-densities are likely to have no significant effects on the crushing performance of the honeycomb structure. For PETG honeycomb structure as shown in Figure 8(d), most of the subsequent peaks are slightly higher than the IPF. This attribute makes the structure also promising as energy absorber. It is seen from the force-displacement curve that up to 5% and 47-50% deformation loading, the honeycomb structures with the two infill-densities behave in similar way. However, the force-displacement curves resulting from the two infill-densities behave differently during the deformation (i.e. the plateau stage). Generally, the low IPF with respect to the subsequent peak forces observed by PETG honeycomb structure makes it more promising over other polymer-based honeycomb structures. Lastly, for the NCC honeycomb structure as depicted in Figure 8 (e), it can be seen that infill-densities have slight effect on the force-displacement curves. Also, deformations at the plateau stage are more stable than for all the polymer-based honeycomb structures. Moreover, the reduced subsequent peaks observed during the deformation process indicate a highly promising material candidate for energy absorbers.

3.3. Deformation mode

At the onset of loading, in the linear-elastic region, it is observed that all the honeycomb material specimens are characterised by homogenous deformation as evident in the force-displacement curves of Figure 8. However, after this region, unique deformation modes characterised each material specimen as displayed in Table 4. For each material specimen type, two infill-densities were tested. However, the effects of infill-densities on the deformation behaviour of the honeycomb structures are insignificant. It should be recalled that the in-plane loading of the honeycomb structures were performed in the x-direction only as illustrated in Figure 1 (c). However, it should be noted that, for in-plane loading in the y-direction, a slightly different results

could be obtained. The results of the collapsed modes clearly indicate that the types of base materials utilised in fabricating the honeycomb structures influence their collapse behaviour.

Table 4 gives different deformation stages of all the honeycomb structures under compression up to 50% strain. During compression loading, it is observed that the deformation of honeycomb structure made from PLA material commences at a deformation strain of 5% on the top side corner. As the loading progresses up to a deformation strain of 15%, a diagonal L-shape deformation mode becomes evident and characterised by bending/buckling of the cell walls with brittle fracture. Moreover, it was observed that the oscillation in the force-displacement curve of the PLA honeycomb structure is the most noticeable among the other material honeycomb structures as represented in Figure 8(a). This is because, PLA material is relatively more brittle and cracks easily during compression. Hence, causing instability in the plateau region which are carried by large oscillations. At a deformation strain of 35%, the number of buckled cell walls increased along the middle portion of the PLA honeycomb structure. Deformation at the bottom of the PLA honeycomb structures become evident at 42% deformation strain. In the case of ABS, at a deformation strain of 15%, the collapse mode commences at the bottom end of the honeycomb structure and progresses diagonally upward-right in a layer-by-layer manner up to the deformation strain of 50%. An oblique quadrilateral collapse mode was also observed at the bottom end of the collapse honeycomb structure. This kind of deformation mode is also observed with PETG honeycomb structure. However, a difference between it and ABS honeycomb deformation is that deformation progresses diagonally upward-left in a layer-by-layer manner up to the deformation strain of 50%. For the ASA honeycomb structure, the collapse behaviour also commences at the bottom end, and as deformation progresses at 35% deformation strain, a horizontal layer-by-layer deformation at the middle of the structure was observed. The whole deformation process also resulted in an oblique quadrilateral collapse at the bottom end of the crushed ABS honeycomb structure. Lastly, for the NCC structure, at 15% deformation strain, deformation begins immediately before the bottom end of the honeycomb structure and progresses diagonally upward-right in a layer-by-layer manner. At a deformation strain of 35%, deformation continues at the top left corner of the honeycomb structure and then progresses diagonally downward-right. The upper and lower diagonal mode patterns formed at a deformation strain of 50% resulted in an increased oblique quadrilateral deformation mode.

Table 4. Stages of deformation modes for the different honeycomb structural specimens for PLA, ABS, ASA, PETG and NCC, respectively with two infill-densities.
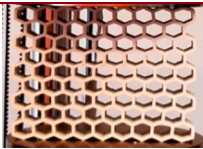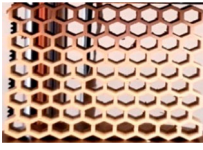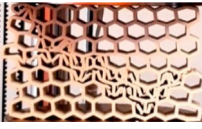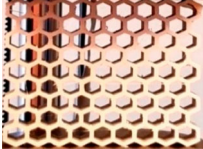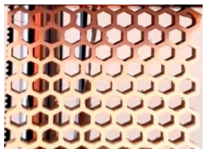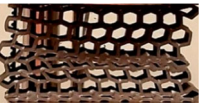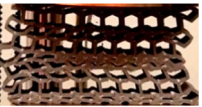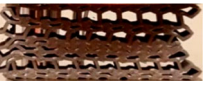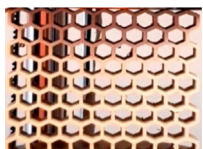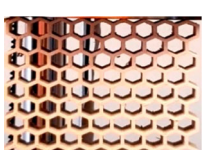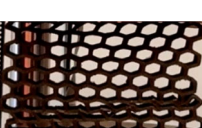
Material/ infill-density		Deformation strain			
		0%	15%	35%	50%
PLA	d_1				
	d_2				
ABS	d_1				
	d_2				
ASA	d_1				
	d_2				
PETG	d_1				
	d_2				
NCC	d_1				
	d_2				

Table 5. Result summary of crushing performance for the different materials utilised to fabricate the honeycomb structures.

Material/ infill-density (%)		EA (J)	SEA (kJ/kg)	MCL (N)	m_c (kg)	m_s (kg)	PCF (N)	CFE (%)
PLA	d_1	257.19	2.53	5143.88	0.10186	0.10318	7957.39	64.64
	d_2	265.09	2.60	5301.84	0.10105	0.10236	8853.25	59.89
ABS	d_1	182.04	2.14	3640.71	0.08498	0.08617	4687.29	77.67
	d_2	184.36	2.16	3687.28	0.08546	0.08666	4687.29	78.67
ASA	d_1	150.93	1.71	3018.61	0.08822	0.08981	4292.14	70.33
	d_2	152.70	1.73	3054.08	0.08833	0.08992	4448.21	68.66
PETG	d_1	263.64	2.50	5272.84	0.10568	0.10674	6564.48	80.32
	d_2	261.98	2.49	5239.53	0.10506	0.10611	6265.11	83.63
NCC	d_1	144.06	2.24	2881.26	0.06431	0.06560	3597.26	80.10
	d_2	147.03	2.30	2940.56	0.06384	0.06512	3949.07	74.46

3.4. Crushing performance

The crashworthiness performance of the crushed honeycomb structure is used to characterise the actual performance of the energy absorbing structure. In this study, one critical parameter considered is the crushed mass m_c of the structure at 50% deformation. When compared with the measured mass (m_s) of the structures before loading with that after 50% deformation, it was observed that the mass of the latter reduced slightly over the former within the range of 1–2% mass reduction. This slight difference in mass is presented in Table 5. To measure the SEA, the mass difference can be ignored especially when the material used for designing the energy absorbing structure is the same. Therefore, the SEA has been measured preferably by various research works using the mass of the structure before loading to the mass of the structure after the deformation stage.

In Figure 9(a), it is seen that the infill-densities have little or no influence on the SEA of the structural honeycombs. However, for the two infill-densities, the
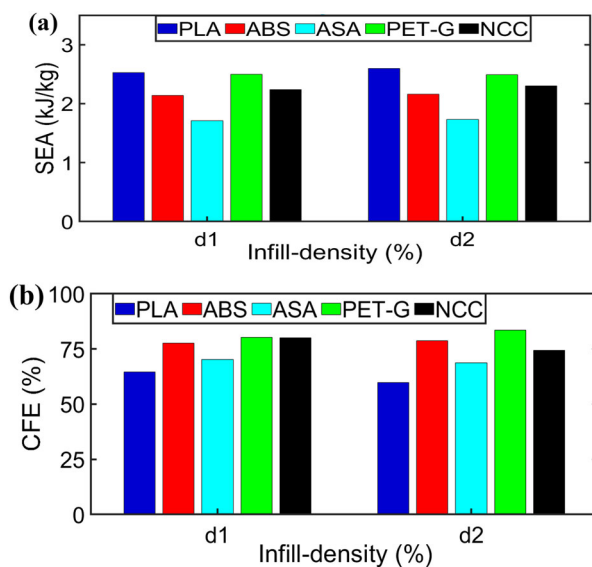
structural honeycomb made from PLA and PETG produce the highest SEA values. The results are attributed to the high energy absorption capacity they produced during and after crushing. For example, for the infill-density d_1, the SEA value of the honeycomb structure made from PETG is 14.40%, 31.60% and 10.4% higher than those made from ABS, ASA and NCC, respectively. In the same vein, for the infill-density d_2, the SEA value of the honeycomb structure made from PETG is 13.25%, 30.52% and 7.63% more than those made from ABS, ASA and NCC, respectively. However, for the infill-densities d_1 and d_2, the SEA values of PLA honeycomb structure are 1.19% and 4.23% slightly higher than that of PETG honeycomb structure. Moreover, it is seen that the ASA honeycomb structural candidate produced the least SEA values which makes them not too promising for energy absorbers. Therefore, given the choice of selecting from these various materials and considering applications strictly demanding higher specific energy absorption, the PLA or PETG structural candidates are most promising.

Figure 9(b) shows the overall crush load efficiency of the various honeycomb structural specimens. It is seen that the infill-densities have little influence on the CFE of the structural honeycomb especially those that are composite-based. For example, the CFE of NCC honeycomb structure at 20% infill-density is approximately 7% higher than the one with 40% infill-density. Similarly, the CFE of PLA at 20% infill-density is 1.08% lower than that at 40% infill-density, while the CFE of ASA at 20% infill-density is 2.38% higher than that at 40% infill-density. On the other hand, increasing the infill-density from 20% to 40% resulted in appreciable increase in the CFE. For example, it can be seen in Table 5 that ABS and PETG honeycomb structures at 40% infill-density are 10.6% and 3.86% higher, respectively than those fabricated with 20% infill-density. A comparison of the overall CFE of all the structural honeycombs shows that those made from PLA material give the least CFE in spite of their high energy absorption capacity. This is because, the CFE index takes into consideration the peak forces of the deformed structures.

Figure 9. Comparison of the crushing performance against infill-densities for the various honeycomb structures (a) specific energy absorption, SEA (b) crush force efficiency, CFE.

Table 6. Comparison of the final mean crushed lengths of the honeycomb structures at d_1 and d_2 for all materials considered in this study.

Material	Crushed length (mm)	
	d_1	d_2
PLA	62.54	62.60
ABS	72.10	74.34
ASA	78.10	78.53
PETG	65.05	65.06
NCC	67.20	67.31

3.5. Effect of crushed length upon deformation

All the materials respond differently after the 50% deformation strain upon the release of the upper platen.
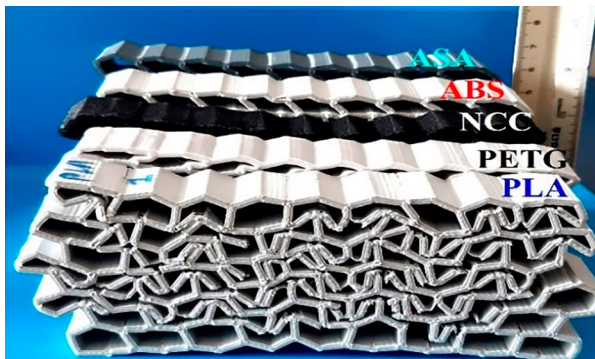

Figure 10. Comparison of the final mean crushed length of 3D printed honeycomb structures with various materials.

Table 6 compares the mean crushed length of the deformed honeycomb structure with d_1 and d_2 after the removal of the moving platen. As depicted in Figure 10, it is seen that ASA honeycomb structure generates the highest in-plane spring up behaviour followed by ABS and then NCC structure. The high spring up behaviour of ASA honeycomb structure could be attributed to the high internal energy retained during the deformation process. The higher the internal energy of the crushed structure, the lower the energy absorbed, and vice versa. This explains why both the PLA and PETG honeycomb structures with lower internal energy, give more promising energy absorption capacities than those of NCC, ABS and ASA honeycomb structures (i.e. see Table 5).

3.6. Effect of material types on macrostructural cell wall deformation

Figure 11 shows the macrostructural collapse behaviour of the honeycomb structures made from the different materials. It can be seen that two of the honeycomb structures i.e. those made from PLA and NCC, undergo a dominant brittle fracture as shown in Figure 11(a) and 11(e), respectively. In this case, the cell walls fracture at their plastic hinges and collapse into their unit cells. In the case of ASA, brittle fracture is dominant at the plastic hinges with bending of the cell walls as shown
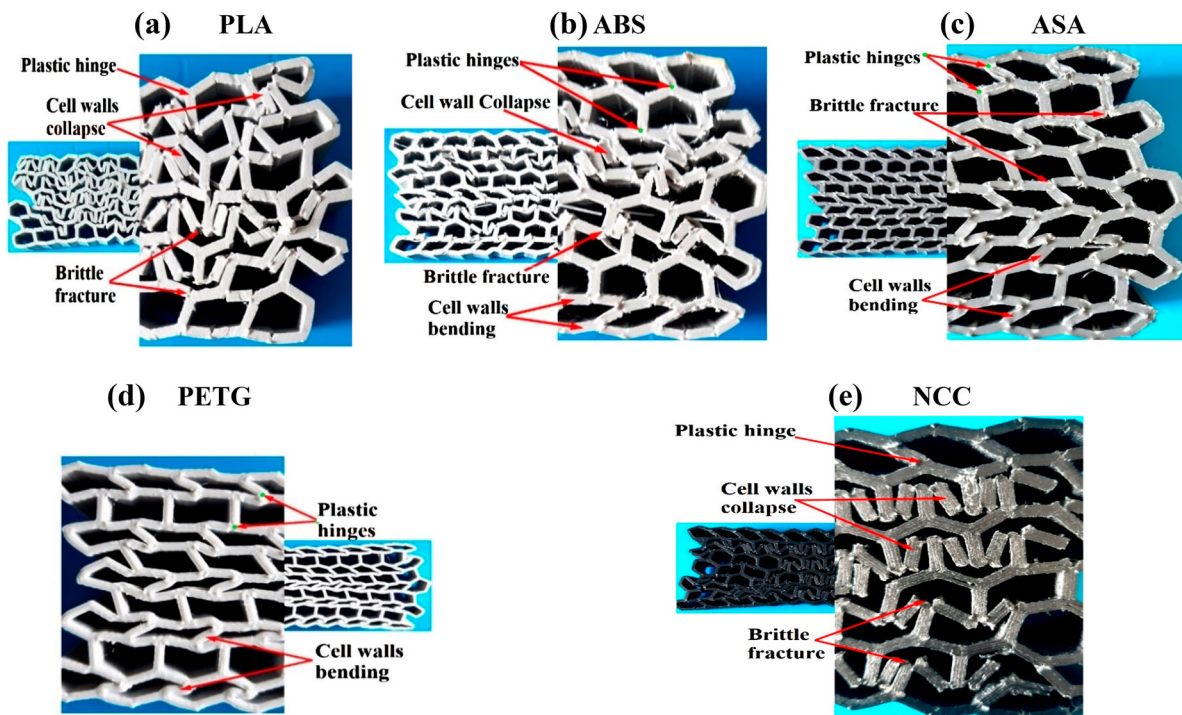

Figure 11. Macrostructure cell walls deformation of honeycomb structures made from different materials (a) PLA (b) ABS (c) ASA (d) PETG (e) NCC.

in Figure 11(c). Moreover, when deformed further, it was observed that ASA honeycomb structure fractures along the cell wall. It is worth nothing that, during the deformation of most of the honeycomb structures characterised by brittle fracture, their initial peak forces was observed to be very high compared to their subsequent peak forces. Consequently, resulting in a low crush force efficiency. However, due to the carbon content in NCC honeycomb structure, the initial peak compared to the subsequent peaks in the load-deformation curve is reduced. However, during the collapse process of honeycomb structures made from PETG, it was observed that the cell walls bend without fracture at their plastic hinges as shown in Figure 11(d). This shows the ductile nature of PETG material. A further compression of PETG honeycomb structure produce a ductile collapse behaviour without hinges or cell-wall fracture. In the case of honeycomb structure made from ABS, it is seen in Figure 11(b) that its collapse behaviour is characterised by both bending along the cell walls and brittle fracture at the plastic hinges with some of the cell walls collapsing into their unit cells. Also, fracture along the cell walls can be observed. The crushing behaviour of ABS honeycomb structure (i.e. bending of the cell walls and fracture at the plastic hinges) accentuates the attribute of it switching from ductile to brittle making it possess higher *CFE* over ASA and PLA honeycomb structures (i.e. see Table 5).

4. Numerical results and verification

In this section, finite element (FE) simulation is performed to compare with the experimental results and give more findings into the crushing performance as well as mechanical behaviour of the honeycomb structures with different materials. It was observed from the experiment that the dependence on different infill-densities to the collapse mode of the honeycomb structure is very weak. Therefore, it does not provide a significant contribution to the crushing mode of the structural

honeycomb made from the same material constituent. In the light of this and to avoid repetition of results, only the mechanical parameters for the infill-density, d_2, was used in the FE approximations to compare with the experimental results.

4.1. Finite element model description

In-plane compression of the various honeycomb structures were performed using the Abaqus/Explicit FE simulation software. First, the honeycomb structure was placed between a moving impactor and a rigid wall as shown in the crushing model of Figure 12(a). It should be noted that the boundary condition of the impactor was fixed in the x and y-directions and made to move in the z-direction. However, the rigid wall was fixed in all the degrees of freedom to avoid translation and rotation during the deformation process. Both the impactor and the rigid wall were modelled as 3D analytical rigid shell elements which required no mesh for result analyses. The material model used for the simulation was elastic-perfectly plastic which is typical for polymeric materials. To further simplify the simulation process and reduce computational time, the FE model assumes no fracture damage on the cell walls of the honeycomb structural models. Hence, damage model of the honeycomb structure in the FE model was not considered for the present study [47]. Moreover, the honeycomb structure was meshed using a 4-node linear tetrahedron element, C3D4. The meshed honeycomb structure and its deformed mesh during in-plane loading are illustrated in Figure 12(b) and (c), respectively.

To further reduce computational time and maintain the quasi-static loading response of the simulation, a velocity (V_z) of 0.15 m/s was adopted to scale up the speed of 2 mm/min utilised in the experiment [48]. The kinetic energy as a result of this velocity scaling tends toward zero and was far less than the internal energy. As in the experiment, the maximum crushing distance was
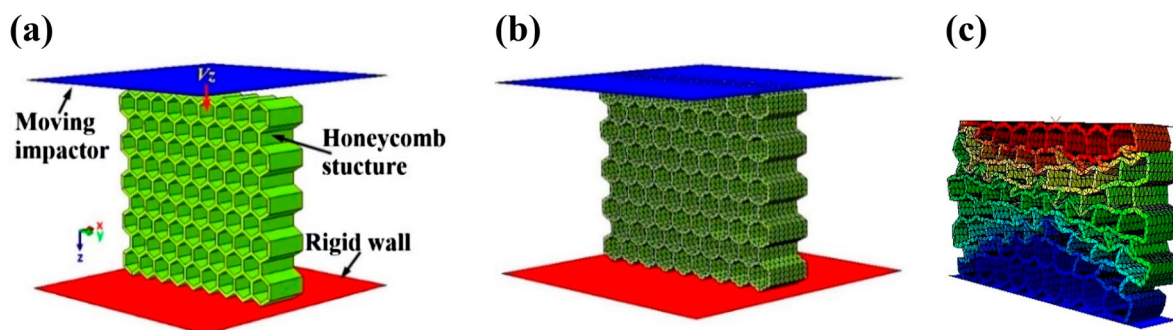

(a)   **(b)**   **(c)**

Figure 12. Honeycomb structural model and FE analysis (a) model description (b) finite element meshing of honeycomb structure (c) illustration of deformed meshes during quasi-static loading of the honeycomb structure.

set for 50 mm to avoid the densification stage. Also, to address self-contact penetration, a general contact was adopted. Tie constraint between the impactor and the honeycomb structure as well as between the rigid wall and the honeycomb structure was ensured using penalty friction for the tangential behaviour and hard contact for the normal behaviour. The total number of tie constraints with material-contact interaction property was thirty-six. The material-contact interaction property ensures the unique deformation mode of the honeycomb structures with different materials. The friction coefficients in the contact interfaces of PLA, ABS, ASA, PETG and NCC honeycomb model for the tangential behaviour were set as 0.42, 0.35, 0.05, 0.22 and 0.35, respectively [49–52]. These friction coefficients can be obtained by a tilted plane test as demonstrated by Ma et al. [53].

Using the PETG honeycomb structure (i.e. the material structure with the best *CLE* as observed from the experiment), a mesh convergence study was carried out to determine the best mesh size and eliminate mesh sensitivity. The mesh sensitivity study of three average element sizes (i.e. 2.4, 3.2 and 4.0 mm) showed that the approximate element size of 3.2 mm with 31,988 elements produced the best convergence as represented in the force-displacement curves, energy-displacement curves and energy-element size curve of Figure 13. The energy-displacement curve history in Figure 13(b) depicts how the energy absorption of both the mesh sizes, 2.4 and 3.2 mm, become approximately equal

despite the shorter computational time of the latter compared to the former. Hence, with the element size of 3.2 mm, more energy was absorbed within acceptable computational time compared to using element size of 4.0 mm as represented in Figure 13(c). Therefore, the element size 3.2 mm, was used for all the FE model of the honeycomb structures made from the different materials. Moreover, Figure 13(a) also gives a good correlation of the force-displacement curves between the PETG honeycomb structure obtained during the experiment and the PETG honeycomb structure for various element sizes obtained in the finite element model. It is worth noting that the brittle fractures observed in some of the honeycomb structures during the experiment was not modelled in the numerical simulation.

4.2. Finite element and deformation modes comparison

The approximations obtained in the numerical method relate well with the experimental results. Table 7 compares the deformation modes of the FE approximations with the experimental results for the honeycomb structures with various materials. In the experiment, brittle fractures occurred at the plastic hinges of the honeycomb structures. However, in the numerical approximations, there are no fractures at the plastic hinges because such fracture conditions were not modelled in the present study but could be considered in future works. The fracture discrepancy causes a slight
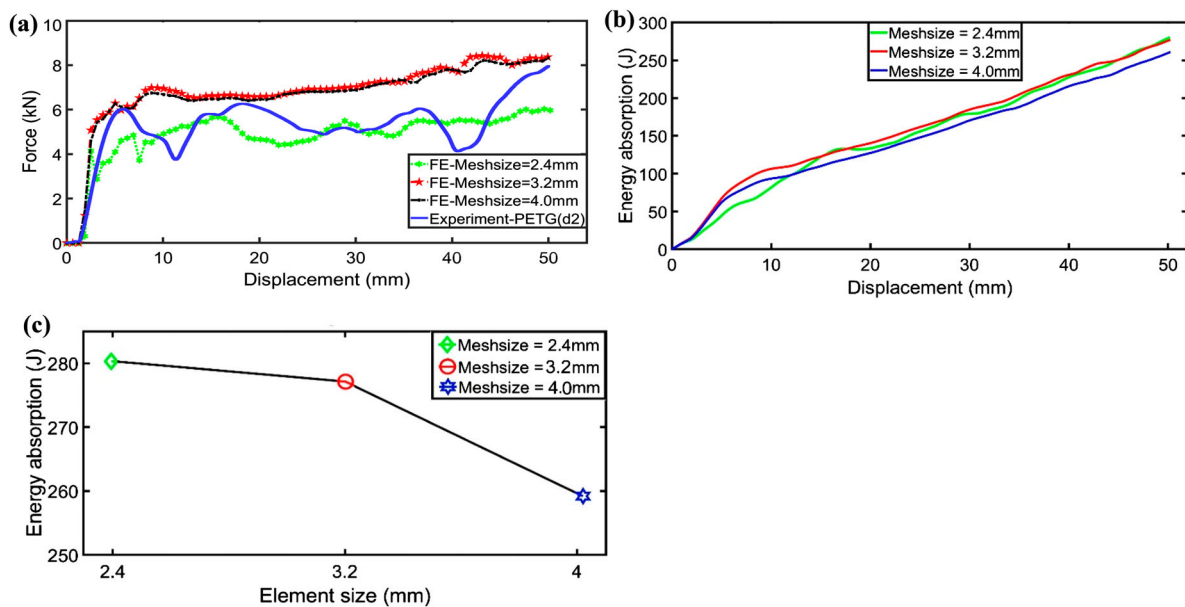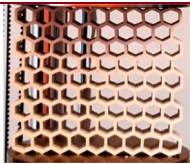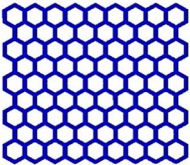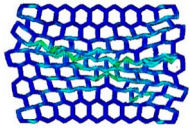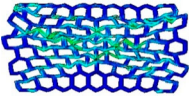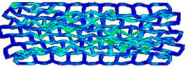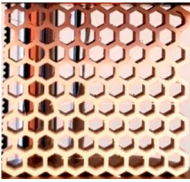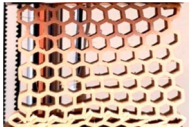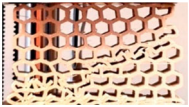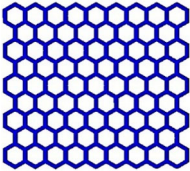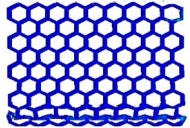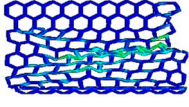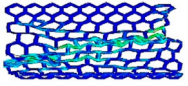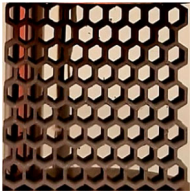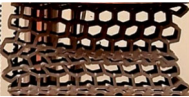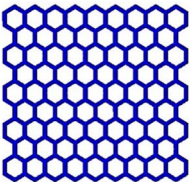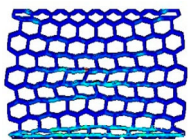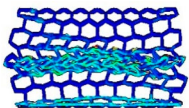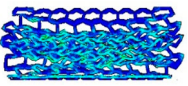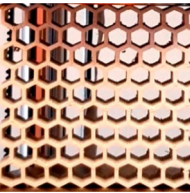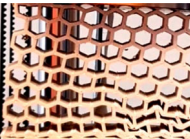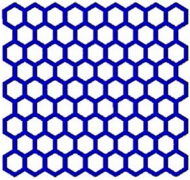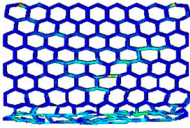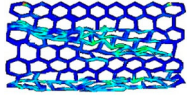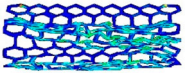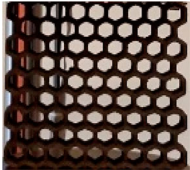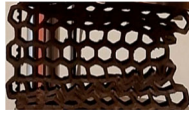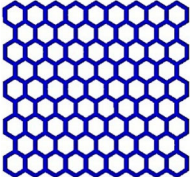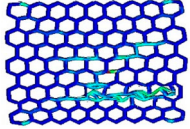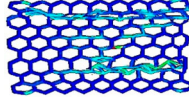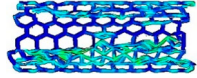

Figure 13. Mesh convergence study of PETG honeycomb structural model (a) comparison of the force-displacement curves between three different average mesh sizes and results obtained by experimental measurement (b) comparison of energy absorption versus displacement curve history for the three average mesh sizes. (c) comparison of energy absorption capacity for the three average mesh sizes.

Table 7. Finite element and experiment comparison of deformation modes of the honeycomb structure made from various materials and at different deformation strains.

Material	Method	Deformation strain			
		0%	15%	35%	50%
PLA	Experiment				
	FE Simulation				
ABS	Experiment				
	FE Simulation				
ASA	Experiment				
	FE Simulation				
PETG	Experiment				
	FE Simulation				

(*Continued*)

Table 7. Continued.

Material	Method	Deformation strain			
		0%	15%	35%	50%
NCC	Experiment				
	FE Simulation				

difference between the deformation modes of the experiment and the simulation. For example, for the PLA honeycomb structure in Table 7, a V-shape band was observed at 15% deformation strain during the experiment. However, this was not evident at the 15% deformation strain in the simulation. In general, at all represented deformation strains as indicated in Table 7, the numerical results approximated well with the experimental measurements.

4.3. Finite element crushing performance comparison

The major crushing performance of the FE approximations and their comparison with the experimental results are represented in Figure 14. Figure 14(a) compares the force displacement graphs between simulation (i.e. Sim) and experiment (i.e. Exp). It can be observed that subsequent peak forces are visible in the experimental
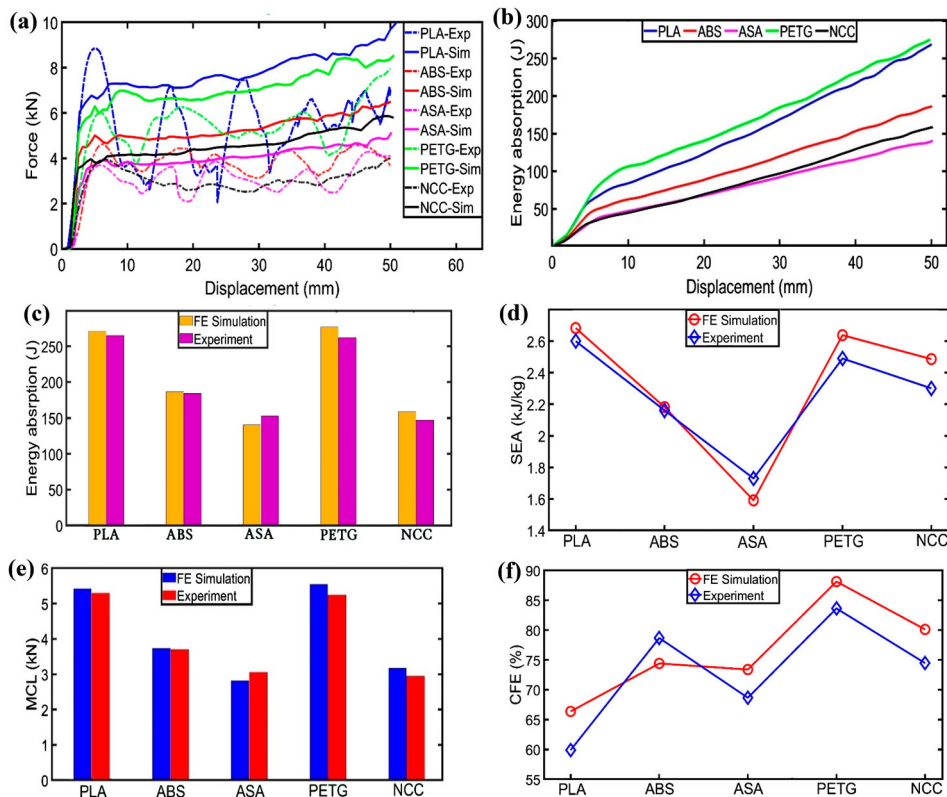
Figure 14. Finite element crushing performance for the honeycomb structural models (a) force-displacement curve comparison between FE simulation and experimental results (b) energy absorption versus displacement curve for simulation results (c) energy absorption comparison between simulation and experiment (d) *SEA* comparison between simulation and experiment (e) *MCL* comparison between simulation and experiment (f) *CFE* comparison between simulation and experiment.

results due to folding and fracture collapse of the cell wall during crushing of the honeycomb structures. However, in the FE simulation results, apart from the initial peak forces observed for the various structural models, the subsequent peak forces are not visible because fracture damage was not modelled during the FE simulation. Also, Figure 14(b) shows the history of the FE force-displacement graphs. Moreover, it can be seen from the force-displacement curves of the simulation that the initial peak forces for all the polymer-based and composite-based honeycomb structures are relatively lower than their maximum peak forces. This shows the promising crushing attributes of polymer and composite materials for crashworthiness applications. The area under the force-displacement curves for the various honeycomb structures represent the energy absorption. It can be observed that more energy is absorbed by PLA and PETG honeycomb structures compared with the ABS ASA and NCC honeycomb structures. Also, it is seen that the energy absorption capacity of ASA and NCC structures are very low compared with that of ABS structure. The low absorbed energy has been attributed to the high internal energy stored by these two materials during their deformation processes. In general, the energy absorption capacity obtained by all the different honeycomb structures during the simulation agrees well with those obtained in the experiment as depicted in Figure 14(c). Despite the low energy absorbed by NCC honeycomb structure, a comparison of the simulation and experiment shows that its *SEA* values are higher than those of ABS and ASA honeycomb structures as represented in Figure 14(d). The increased *SEA* value of NCC over ABS and ASA honeycomb structures is probably initiated by the presence of carbon particle/ fibre in its composite. The *SEA* and *MCL* results at infill-density d_2, obtained from both the simulation and experiment for PLA and ABS structures, indicate very close agreement i.e. see Figure 14(d) and (e). Also, in the two evaluation methods, it can be seen in Figure 14(f) that

PETG honeycomb structure has the highest *CFE* and out-performs all others in crushing performance. However, PLA honeycomb structure indicates the lowest *CFE* results both numerically and experimentally. This could be attributed to its highly brittle nature as seen in its macro-structural behaviour during mechanical crushing.

5. Analytical prediction and verification

In this section, the theoretical solution of the mean crushing strength of honeycomb unit cell influenced by the flow stress of the parent materials, as described in this work, is calculated and compared with the FE approximations.

5.1. Theoretical mean crushing strength

For the honeycomb unit cell, there are four inclined cell walls and two vertical cell ones. Owing to small deflection, it is assumed that the unit cell walls exhibit a Euler-Bernoulli beam characteristics with uniformly distributed load acting on the unit cell along the *x*-direction. Moreover, it is assumed theoretically that the deformation of the vertical cell walls is not taking into consideration and can be ignored [54,55]. However, due to the in-plane compression under quasi-static loading i.e. as depicted in Figure 15(a), the inclined cell walls are assumed to undergo bending deformation theoretically. Figure 15(b) gives the free body diagram of the bending of one of the cell walls of the unit cell inclined at AB. The cell wall material is modelled as elastoplastic. During in-plane compression loading, the stress components are zero and the bending moments due to the forces *F* acting on the beam as illustrated in Figure 15(b) is given by

$$M = \frac{1}{2}Fl\cos\theta \tag{7}$$

The deflection δ of the cell wall beam is calculated as $\delta = Ml^2/6E_ml$. Where E_m is the Young's modulus of the

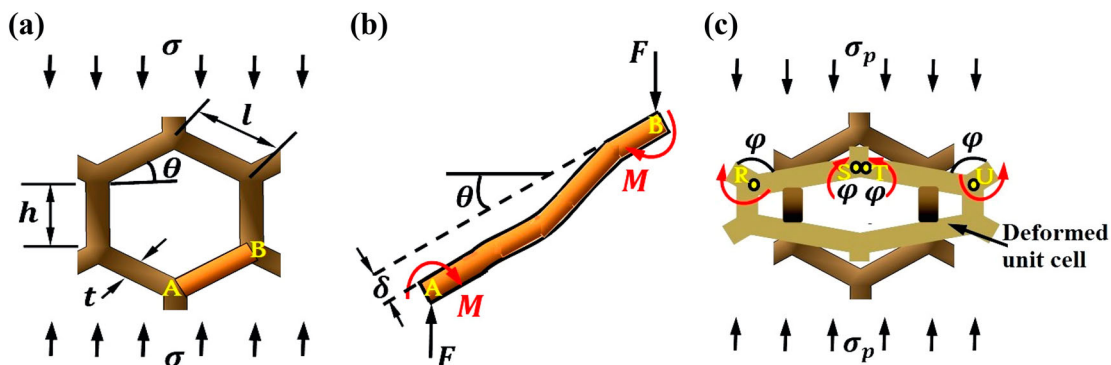**Figure 15.** (a) conventional hexagonal honeycomb unit cell under in-plane stress and showing the inclined cell wall (b) free-body diagram of the inclined cell wall and its deflection due to bending and forces acting on the cell wall (c) plastic deformation under in-plane crushing and resulting in the plastic rotation of the hinges.

parent materials (i.e. PLA, ABS, ASA, PETG and NCC) which is given in Table 3. As performed in the simulation, only the material properties obtained using infill-density d_2 is used for the theoretical analysis. Also, the symbol $I = a_z t^3/12$, denotes the moment of inertial which is assumed to be the same for all the honeycomb structures with different parent material constituents used in the study. Where a_z represent the out-of-plane width of the honeycomb unit cell obtained along the z-direction of printing. Hence, the strain ε due to the deflection of the honeycomb unit cell wall beam in the in-plane crushing direction can be obtained.

Figure 15(c) shows the plastic deformation of the cell walls due to in-plane compressive loading. This occurs at a point where the bending moment of the cell wall equals the plastic moment [56,57]. The external work imposed on the honeycomb unit cell is given by

$$W_{ext} = Fa_z = \frac{3\sqrt{3}}{2}\sigma_p l^2 a_z \tag{8}$$

where σ_p is the maximum collapse strength. The plastic dissipation at the four hinges is given as

$$W_p = 4M_p\varphi \tag{9a}$$

where φ is the plastic rotation at the hinges as shown in Figure 15(c). In this study, φ is taken as $2\pi/5$. Also, the term $M_p = \sigma_0 a_z t^2/4$ is the plastic bending moment of the cell wall. Equation 9(a) becomes

$$W_p = \frac{2\pi}{5}\sigma_0 a_z t^2 \tag{9b}$$

The honeycomb unit cell collapse when the external work acting on the unit cell equals the plastic dissipation at the four hinges. Hence, the maximum collapse stress can be obtained as

$$\sigma_p = \frac{4\pi}{15\sqrt{3}}\sigma_0\left(\frac{t}{l}\right)^2 \tag{10}$$

where the ratio t/l is considered as the slenderness of the honeycomb cell wall. Moreover, the mean crushing stress σ_{mean} is the average collapse stress during the plastic deformation process and can be obtained by

the expression,

$$\sigma_{mean} = \frac{\sigma_p}{\varepsilon_{max}} \tag{11}$$

The symbol, ε_{max}, is the maximum crushing strain whose value was determined as 0.5 at the onset of densification during the experimental and numerical simulation procedures.

5.2. Theoretical verification

The theoretical results are verified with the FE approximations by comparing their *SEA* values. The *SEA* crushing index is related to the mean crushing stress and density of the parent material (ρ_m) by the equation,

$$SEA = \frac{\sigma_{mean}}{\rho_m} \tag{12}$$

where the density of the parent material is given in Table 3. It can be seen from Figure 16 that the theoretical results are similar to the FE approximations. The theoretical *SEA* and energy absorption values for both PLA and ABS models are higher than their simulation values. Moreover, it is seen that the theoretical *SEA* and energy absorption values for both ASA and NCC models are approximately the same. However, for PETG models, the theoretical *SEA* and energy absorption values are lower than the simulation values. Furthermore, the maximum *SEA* and energy absorption values are obtained by the honeycomb structural models made from PLA and PETG materials. The least *SEA* value is obtained by those made from ASA material. While the *SEA* values of NCC structural model for both the theory and simulation give very similar results, it can be observed that NCC model are relatively higher than the ABS and ASA models in terms of *SEA* values. Lastly, the energy absorbed by the NCC model for both the theoretical and FE simulation, is relatively low as that of the ASA model depicted in Figure 16(b).

Table 8 shows the error due to theoretical deviation from the simulation and experiment. It can be seen that both the theoretical and simulation results have
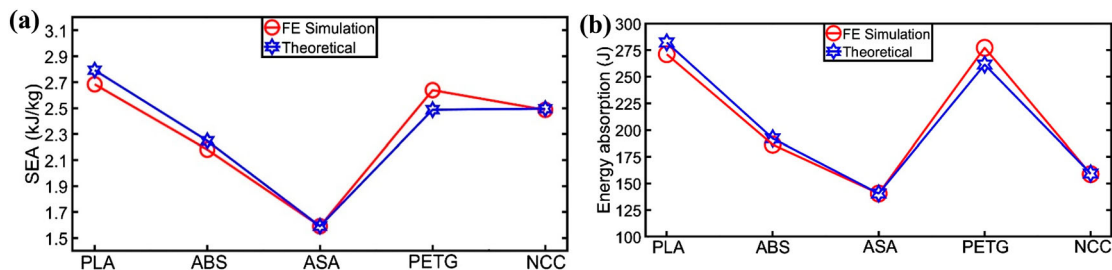
Figure 16. Comparison between theoretical solution and FE approximations (a) SEA performance (b) Energy absorption capacity.

Table 8. Comparison of the *SEA* between theoretical and FE simulation and between theoretical and experimental results.

Structural model	SEA (kJ/kg)			SEA (kJ/kg)		
	Theory	FE	Error (%)	Theory	Experiment	Error (%)
PLA	2.792	2.683	−3.90	2.792	2.60	−6.88
ABS	2.248	2.181	−2.98	2.248	2.16	−3.91
ASA	1.591	1.591	0.00	1.591	1.73	8.74
PETG	2.488	2.638	6.02	2.488	2.49	0.08
NCC	2.495	2.486	−0.36	2.495	2.30	−7.82

very close similarity. The slight difference between these two results can be attributed to the choice of plastic rotation given for the theoretical calculation. The influence of this parameter is analysed in the next subsection. Moreover, it is evident from Table 8 that the maximum *SEA* error of the theoretical deviation with respect to the simulation and experiment are 6.02% for PETG model and 8.74% for ASA model,

respectively. Similarly, the minimum *SEA* error of the theoretical deviation with respect to the simulation and experiment are 0.0% for the ASA model and 0.08% for the PETG model, respectively. These maximum and minimum error values indicate that the theoretical model is within reasonable solution and can be satisfactorily used to compare both the FE simulation and experimental results.
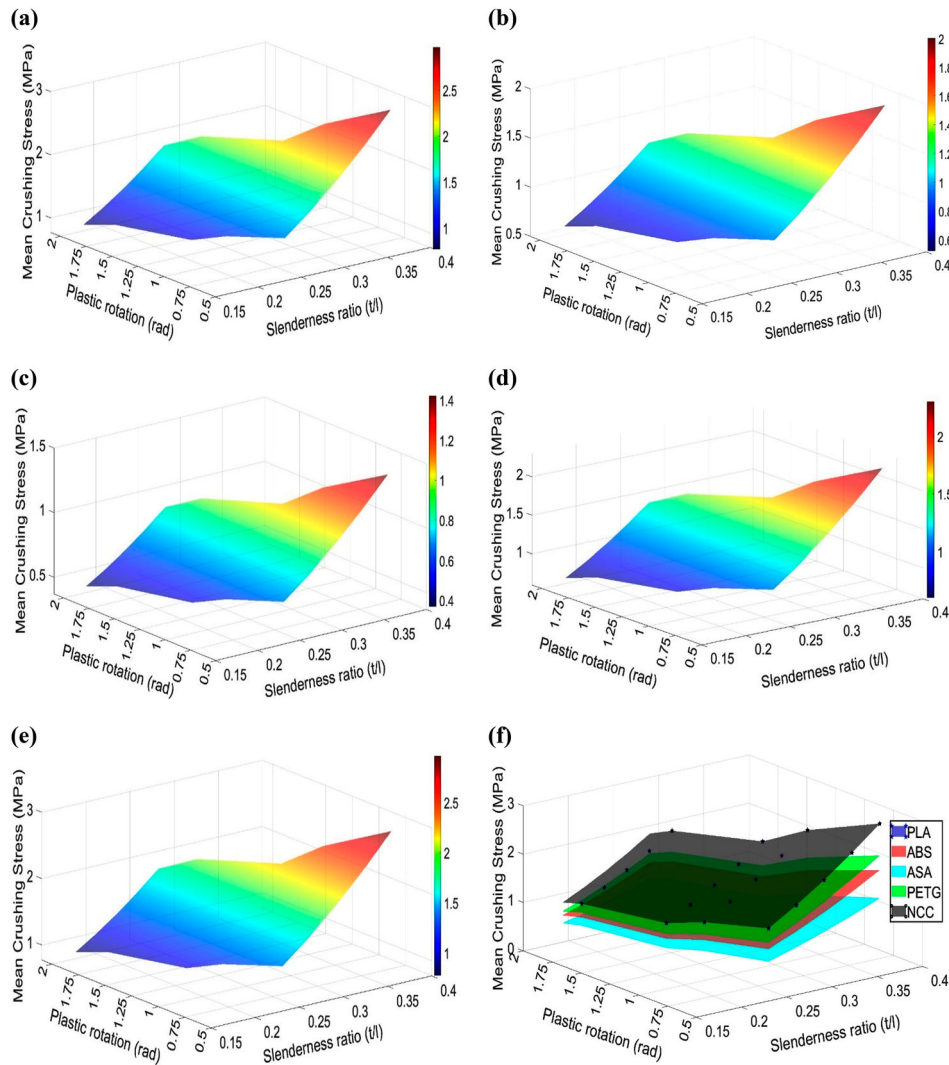
Figure 17. Influence of plastic rotation of hinges and slenderness ratio on the mean crushing stress for (a) PLA model (b) ABS model (c) ASA model (d) PETG model (f) NCC model (g) comparison of the honeycomb structural models obtained from different materials.

5.3. Parametric analysis

In Equation (12), the higher the mean crushing strength (σ_{mean}) the better the energy absorbed per unit mass of the crushed structure, i.e. the *SEA* value of the crushed honeycomb structure increases. However, during plastic deformation of the honeycomb structure, the plastic rotation at the hinges (φ) and the slenderness ratio of the cell wall (t/l) are key parameters that influence the crushing performance. Figure 17 combines the effect of φ and t/l on σ_{mean} for all the structural models made from various materials. Five φ (i.e. in radians) including $\pi/5$, $\pi/3$, $2\pi/5$, $3\pi/5$ and $2\pi/3$ are used. Also, thicknesses and cell wall lengths ranging from 1.6 mm to 2.4 mm with 0.2 mm intervals, and 6.5 mm to 8.5 mm with 0.5 mm intervals, respectively, are considered. From Figure 17, the results show that as the slenderness ratio increases, the σ_{mean} increases. However, there is a non-linear decrease of σ_{mean} with increased plastic rotation. The maximum values of σ_{mean} for all structural models are obtained when $t = 2.4$ mm, $l = 6.5$ mm and $\varphi = 0.63$ radians. Also, the minimum values of σ_{mean} for all structural models are obtained when $t = 1.6$ mm, $l = 8.5$ mm and φ rises to 2.094 radians. For PLA model in Figure 17(a), the optimum and minimum σ_{mean} are 2.96 and 0.77 MPa, respectively. In the case of ABS model as shown in Figure 17(b), the optimum and minimum σ_{mean} are 2.00 and 0.52 MPa, respectively. Moreover, ASA model has optimum and minimum σ_{mean} at 1.42 and 0.37 MPa, respectively as seen in Figure 17(c). The ASA model is the least desired for energy absorption. For PETG model, (i.e. see Figure 17(d)), the optimum and minimum σ_{mean} occurs at 2.30 and 0.60 MPa, respectively. Lastly, for the NCC model shown in Figure 17(e), the maximum value of σ_{mean} is obtained at 2.97 MPa while the minimum value is obtained at 0.77 MPa. These analyses indicate that NCC, PLA and PETG models are promising candidates that can produce improved *SEA* performance by obtaining the optimum values of σ_{mean} as depicted in Figure 17(f). The theoretical prediction of optimum structural designs for the various materials is, therefore, a veritable means of preventing waste of materials which are usually encountered during experimental procedure and fabrication process. Therefore, by careful selection of parameters, it is plausible to improve both the mechanical and crushing performances of honeycomb structure and other complex design use to generate energy absorbing structures.

6. Conclusion

The mechanical properties and crashworthiness performance of energy absorbing honeycomb structures made from four polymer-based materials and one polymer-fibre reinforcement material, have been investigated. These structures were manufactured via the FFF technology and compressed under in-plane quasi-static loading condition. Experimental results correlate well with both the FE approximations and analytical prediction. In general, the investigation showed that the type of materials used in FFF 3D printed honeycomb structures can influence the deformation modes and overall crashworthiness performance of energy absorbing structures. In addition to the novelty of the study in that it characterised different materials, revealed their material microstructures and compared their macrostructural in-plane crushing performance at the same time, the following also enumerates other main findings of the study:

1. Under various deformation strains, unique failure modes for the studied honeycomb structures with different materials were observed in the experiment and simulation. Moreover, the macrostructure deformation revealed that PLA structure was brittle, ABS structure could switch from being brittle to being ductile, ASA structure had ductile property, PETG structure was more ductile than brittle and lastly, NCC structure was brittle.
2. Results showed that in terms of the *CFE*, the honeycomb structures made from PETG outperformed those made from PLA by 39.64%; ABS by 6.30%; ASA by 21.80% and NCC by 12.32%. PLA structure produced the least *CFE* due to its highly brittle nature compared to other material counterparts.
3. Also, in terms of both *EA* and *SEA*, the PETG honeycomb structure was approximately equal to that of PLA honeycomb structure. These two honeycomb structures (i.e. those made from PETG and PLA) showed higher *EA* and *SEA* values than those made from ABS, ASA and NCC. However, NCC honeycomb structure outperformed ABS and ASA honeycomb structures in *SEA* values.
4. Investigation also revealed the characteristic lightweight advantage of NCC honeycomb structure over the polymer-based ones. The lightweight advantage of NCC honeycomb structure could be attributed to the fiber reinforcement in the composite material which were obviously absent in the polymer-based honeycomb structures. NCC structures can, therefore, be utilised for crashworthiness application especially where extreme lightweight property is highly desired.

Disclosure statement

ORCID

Chukwuemeke William Isaac ⓘ http://orcid.org/0000-0003-1501-8468

References

[1] Kies F, Köhnen P, Wilms MB, et al. Design of high-manganese steels for additive manufacturing applications with energy-absorption functionality. Mater Des. 2018;160:1250–1264. doi:10.1016/j.matdes.2018.10.051

[2] Wang P, Yang F, Li P, et al. Design and additive manufacturing of a modified face-centered cubic lattice with enhanced energy absorption capability. Extreme Mech Lett. 2021a;47:101358. doi:10.1016/j.eml.2021.101358

[3] Schneider J, Schiffer A, Hafeez F, et al. Dynamic crushing of tailored honeycombs realized via additive manufacturing. Int J Mech Sci. 2022;219:107126. doi:10.1016/j.ijmecsci.2022.107126

[4] Isaac CW. Crashworthiness performance of green composite energy absorbing structure with embedded sensing device providing cleaner environment for sustainable maintenance. Sustain Mater Technol. 2020;25:e00196. doi:10.1016/j.susmat.2020.e00196

[5] Li C, Lei H, Zhang Z, et al. Architecture design of periodic truss-lattice cells for additive manufacturing. Addit Manuf. 2020;34:101172. doi:10.1016/j.addma.2020.101172

[6] Isaac CW. Crushing response of circular thin-walled tube with non-propagating crack subjected to dynamic oblique impact loading. Int J Protective Struct. 2020;11(1):41–68. doi:10.1177/2041419619849087

[7] Linforth S, Ngo T, Tran P, et al. Investigation of the auxetic oval structure for energy absorption through quasi-static and dynamic experiments. Int J Impact Eng. 2021;147:103741. doi:10.1016/j.ijimpeng.2020.103741

[8] Xu A, Saleh M, Bhattacharyya D. Experimental and computational analysis of the in situ tensile deformation of 2D honeycomb lattice structures in Ni single crystals. Compos Part B: Eng. 2020;186:107823. doi:10.1016/j.compositesb.2020.107823

[9] Pehlivan L, Baykasoğlu C. An experimental study on the compressive response of CFRP honeycombs with various cell configurations. Compos Part B: Eng. 2019;162:653–661. doi:10.1016/j.compositesb.2019.01.044

[10] Jiang F, Yang S, Ding C, et al. Quasi-static crushing behavior of novel circular double arrowed auxetic honeycombs: experimental test and numerical simulation. Thin-Walled Struct. 2022;177:109434. doi:10.1016/j.tws.2022.109434

[11] Tao Y, Li P, Zhang H, et al. Compression and flexural properties of rigid polyurethane foam composites reinforced with 3D-printed polylactic acid lattice structures. Compos Struct. 2022;279:114866. doi:10.1016/j.compstruct.2021.114866

[12] Choy SY, Sun CN, Leong KF, et al. Compressive properties of Ti-6Al-4 V lattice structures fabricated by selective laser melting: design,: orientation and density. Additive Manufacturing. 2017;16:213–224. doi:10.1016/j.addma.2017.06.012

[13] Liang H, Hao W, Xue G, et al. Parametric design strategy of a novel self-similar hierarchical honeycomb for multi-stage energy absorption demand. Int J Mech Sci. 2022;217:107029. doi:10.1016/j.ijmecsci.2021.107029

[14] Isaac CW, Duddeck F. Current trends in additively manufactured (3D printed) energy absorbing structures for crashworthiness application – a review. Virtual Phys Prototyp. 2022;17(4):1058–1101. doi:10.1080/17452759.2022.2074698

[15] Quan C, Han B, Hou Z, et al. 3d printed continuous fiber reinforced composite auxetic honeycomb structures. Compos Part B: Eng. 2020;187:107858. doi:10.1016/j.compositesb.2020.107858

[16] Guo MF, Yang H, Zhou YM, et al. Mechanical properties of 3D hybrid double arrow-head structure with tunable poisson's ratio. Aerosp Sci Technol. 2021;119:107177. doi:10.1016/j.ast.2021.107177

[17] Li X, Li Z, Guo Z, et al. A novel star-shaped honeycomb with enhanced energy absorption. Compos Struct. 2023;309:116716. doi:10.1016/j.compstruct.2023.116716

[18] Chen Y, Ye L, Han X. Experimental and numerical investigation of zero Poisson's ratio structures achieved by topological design and 3D printing of SCF/PA. Compos Struct. 2022;293:115717. doi:10.1016/j.compstruct.2022.115717

[19] Ebrahimi MS, Hashemi R, Etemadi E. In-plane energy absorption characteristics and mechanical properties of 3D printed novel hybrid cellular structures. J Mater Res Technol. 2022;20:3616–3632. doi:10.1016/j.jmrt.2022.08.064

[20] Wang T, An J, He H, et al. A novel 3D impact energy absorption structure with negative Poisson's ratio and its application in aircraft crashworthiness. Compos Struct. 2021;262:113663. doi:10.1016/j.compstruct.2021.113663

[21] Kucewicz M, Baranowski P, Małachowski J, et al. Modelling and characterization of 3D printed cellular structures. Mater Des. 2018;142:177–189. doi:10.1016/j.matdes.2018.01.028

[22] Bates SR, Farrow IR, Trask RS. 3D printed polyurethane honeycombs for repeated tailored energy absorption. Mater Des. 2016;112:172–183. doi:10.1016/j.matdes.2016.08.062

[23] Siddique SH, Hazell PJ, Wang H, et al. Lessons from nature: 3D printed bio-inspired porous structures for impact energy absorption–A review. Addit Manuf. 2022:103051. doi:10.1016/j.addma.2022.103051

[24] Bogusz P, Popławski A, Stankiewicz M, et al. Experimental research of selected lattice structures developed with 3D printing technology. Materials (Basel). 2022;15(1):378. doi:10.3390/ma15010378

[25] Fatma N, Haleem A, Javaid M, et al. Comparison of fused deposition modeling and color jet 3D printing technologies for the printing of mathematical geometries. J Ind Integration Manage. 2021;6(01):93–105. doi:10.1142/S2424862220500104

[26] Li T, Wang L. Bending behavior of sandwich composite structures with tunable 3D-printed core materials. Compos Struct. 2017;175:46–57. doi:10.1016/j.compstruct.2017.05.001

[27] Niknam H, Akbarzadeh AH. Graded lattice structures: simultaneous enhancement in stiffness and energy absorption. Mater Des. 2020;196:109129. doi:10.1016/j.matdes.2020.109129

[28] Choudhry NK, Panda B, Kumar S. In-plane energy absorption characteristics of a modified re-entrant auxetic structure fabricated via 3D printing. Compos Part B: Eng. 2022;228:109437. doi:10.1016/j.compositesb.2021.109437

[29] Geramizadeh H, Dariushi S, Salami SJ. Optimal face sheet thickness of 3D printed polymeric hexagonal and re-entrant honeycomb sandwich beams subjected to three-point bending. Compos Struct. 2022;291:115618. doi:10.1016/j.compstruct.2022.115618

[30] Sarvestani HY, Akbarzadeh AH, Niknam H, et al. 3D printed architected polymeric sandwich panels: energy absorption and structural performance. Compos Struct. 2018;200:886–909. doi:10.1016/j.compstruct.2018.04.002

[31] Dou H, Ye W, Zhang D, et al. Comparative study on in-plane compression properties of 3D printed continuous carbon fiber reinforced composite honeycomb and aluminum alloy honeycomb. Thin-Walled Struct. 2022;176:109335. doi:10.1016/j.tws.2022.109335

[32] Lalegani Dezaki M, Mohd Ariffin MK, Hatami S. An overview of fused deposition modelling (FDM): research, development and process optimisation. Rapid Prototyp J. 2021;27(3):562–582. doi:10.1108/RPJ-08-2019-0230

[33] Antony S, Cherouat A, Montay G. Fabrication and characterization of hemp fibre based 3D printed honeycomb sandwich structure by FFF process. Appl Compos Mater. 2020;27:935–953. doi:10.1007/s10443-020-09837-z

[34] Farrokhabadi A, Gharehbaghi H, Malekinejad H, et al. Study of equivalent mechanical properties and energy absorption of composite honeycomb structures. Int J Appl Mech. 2023a;15(6):2350038. doi:10.1142/S1758825123500382

[35] Farrokhabadi A, Veisi H, Gharehbaghi H, et al. Investigation of the energy absorption capacity of foam-filled 3D-printed glass fiber reinforced thermoplastic auxetic honeycomb structures. Mech Adv Mater Struct. 2023b;30(4):758–769. doi:10.1080/15376494.2021.2023919

[36] Feng G, Li S, Xiao L, et al. Energy absorption performance of honeycombs with curved cell walls under quasi-static compression. Int J Mech Sci. 2021;210:106746. doi:10.1016/j.ijmecsci.2021.106746

[37] Saufi SA, Zuhri MY, Dezaki ML, et al. Compression behaviour of bio-inspired honeycomb reinforced starfish shape structures using 3D printing technology. Polymers (Basel). 2021;13(24):4388. doi:10.3390/polym13244388

[38] Habib FN, Iovenitti P, Masood SH, et al. In-plane energy absorption evaluation of 3D printed polymeric honeycombs. Virtual Phys Prototyp. 2017;12(2):117–131. doi:10.1080/17452759.2017.1291354

[39] Alomarah A, Masood SH, Ruan D. Out-of-plane and in-plane compression of additively manufactured auxetic structures. Aerosp Sci Technol. 2020;106:106107. doi:10.1016/j.ast.2020.106107

[40] Li T, Sun J, Leng J, et al. Quasi-static compressive behavior and energy absorption of novel cellular structures with varying cross-section dimension. Compos Struct. 2023;306:116582. doi:10.1016/j.compstruct.2022.116582

[41] Domínguez-Rodríguez G, Ku-Herrera JJ, Hernández-Pérez A. An assessment of the effect of printing orientation: density, and filler pattern on the compressive performance of 3D printed ABS structures by fuse deposition. Int J Adv Manuf Technol. 2018;95:1685–1695. doi:10.1007/s00170-017-1314-x

[42] Ma Q, Rejab MR, Kumar AP, et al. Effect of infill pattern: density and material type of 3D printed cubic structure under quasi-static loading. Proc Inst Mech Eng. Part C: J Mech Eng Sci. 2021;235(19):4254–4272. doi:10.1177/0954406220971667

[43] Lubombo C, Huneault MA. Effect of infill patterns on the mechanical performance of lightweight 3D-printed cellular PLA parts. Mater Today Commun. 2018;17:214–228. doi:10.1016/j.mtcomm.2018.09.017

[44] Khosravani MR, Berto F, Ayatollahi MR, et al. Characterization of 3D-printed PLA parts with different raster orientations and printing speeds. Sci Rep. 2022;12(1):1016. doi:10.1038/s41598-022-05005-4

[45] Balawi S, Abot JL. The effect of honeycomb relative density on its effective in-plane elastic moduli: An experimental study. Compos Struct. 2008;84(4):293–299. doi:10.1016/j.compstruct.2007.08.009

[46] Isaac CW, Duddeck F. Recent progress in 4D printed energy-absorbing metamaterials and structures. Virtual Phys Prototyp. 2023;18(1):e2197436. doi:10.1080/17452759.2023.2197436

[47] San Ha N, Pham TM, Tran TT, et al. Mechanical properties and energy absorption of bio-inspired hierarchical circular honeycomb. Compos Part B: Eng. 2022;236:109818. doi:10.1016/j.compositesb.2022.109818

[48] Gong C, Bai Z, Lv J, et al. Crashworthiness analysis of bionic thin-walled tubes inspired by the evolution laws of plant stems. Thin-Walled Struct. 2020;157:107081. doi:10.1016/j.tws.2020.107081

[49] Şirin Ş, Aslan E, Akincioğlu G. Effects of 3D-printed PLA material with different filling densities on coefficient of friction performance. Rapid Prototyp J. 2023;29(1):157–165. doi:10.1108/RPJ-03-2022-0081

[50] Sudeepan J, Kumar K, Barman TK, et al. Study of friction and wear of ABS/Zno polymer composite using Taguchi technique. Proc Mater Sci. 2014;6:391–400. doi:10.1016/j.mspro.2014.07.050

[51] Batista M, Blanco D, Del Sol I, et al. Tribological characterization of fused deposition modelling parts. In: *IOP conference series: materials science and engineering*. IOP Publishing.2021 Oct 1 (Vol. 1193, No. 1, p. 012068).

[52] Difallah BB, Kharrat M, Dammak M, et al. Mechanical and tribological response of ABS polymer matrix filled with graphite powder. Mater Des. 2012;34:782–787. doi:10.1016/j.matdes.2011.07.001

[53] Ma XF, Guo DH, Lu YH. The research of static friction coefficient measure technology and calibration method for traffic engineering. Appl Mech Mater. 2012;128:1493–1496.

[54] Xu M, Liu D, Wang P, et al. In-plane compression behavior of hybrid honeycomb metastructures: theoretical and experimental studies. Aerosp Sci Technol. 2020;106:106081. doi:10.1016/j.ast.2020.106081

[55] Wang AJ, McDowell DL. In-plane stiffness and yield strength of periodic metal honeycombs. J Eng Mater Technol. 2004;126(2):137–156. doi:10.1115/1.1646165

[56] Gibson LJ, Ashby MF. *Cellular solids: structure and properties*, 2nd ed. Cambridge University Press, Cambridge, UK; 1999.

[57] Xu M, Xu Z, Zhang Z, et al. Mechanical properties and energy absorption capability of AuxHex structure under in-plane compression: theoretical and experimental studies. Int J Mech Sci. 2019;159:43–57. doi:10.1016/j.ijmecsci.2019.05.044